

1 **Seismicity Induced by Longwall Coal Mining at the**  
2 **Thoresby Colliery, Nottinghamshire, U.K.**

3 James P. Verdon<sup>1\*</sup>, J-Michael Kendall<sup>1</sup>, Antony Butcher<sup>1</sup>, Richard  
4 Lockett<sup>2</sup>, Brian J. Baptie<sup>2</sup>,

5 *1. School of Earth Sciences, University of Bristol, Wills Memorial Building, Queen's*  
6 *Road, Bristol, U.K., BS8 1RJ.*

7 *2. British Geological Survey, The Lyell Centre, Research Avenue South, Edinburgh,*  
8 *U.K., EH14 4AP.*

9

10 \*Corresponding Author. Email: James.Verdon@bristol.ac.uk, Tel: 0044 117 331 5135.

11

12

13

## ABSTRACT

The U.K. has a long history of deep coal mining, and numerous cases of mining-induced seismicity have been recorded over the past 50 years. In this study we examine seismicity induced by longwall mining at one of the U.K.'s last deep coal mines, the Thoresby Colliery, Nottinghamshire. After public reports of felt seismicity in late 2013 a local seismic monitoring network was installed at this site, which provided monitoring from February to October 2014. This array recorded 305 seismic events, which form the basis of our analysis.

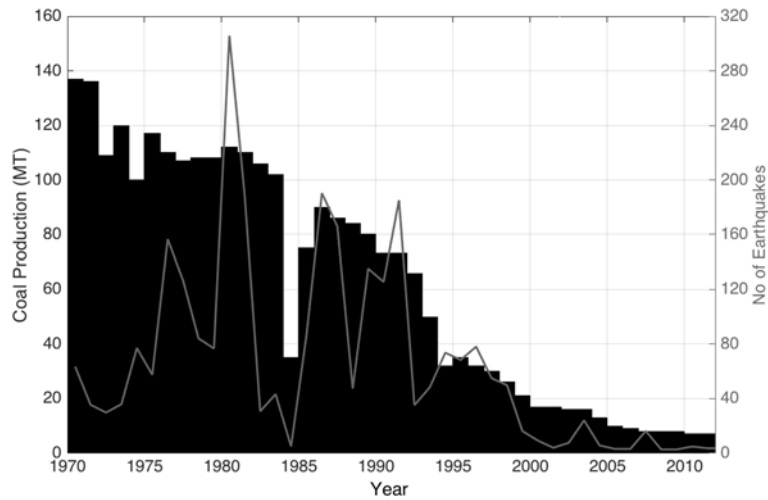
Event locations were found to closely track the position of the mining face within the Deep Soft Seam, with most events occurring up to 300 m ahead of the face position. This indicates that the seismicity is being directly induced by the mining, as opposed to being caused by activation of pre-existing tectonic features by stress transfer. However, we do not observe correlation between the rate of excavation and the rate of seismicity, and only a small portion of the overall deformation is being released as seismic energy.

Event magnitudes do not follow the expected Gutenberg-Richter distribution. Instead, the observed magnitude distributions can be reproduced if a Truncated Power Law distribution is used to simulate the rupture areas. The best-fit maximum rupture areas correspond to the distances between the Deep Soft Seam and the seams that over- and underlie it, which have both previously been excavated. Our inference is that the presence of a rubble-filled void (or goaf) where these seams have been removed is preventing the growth of larger rupture areas.

Source mechanism analysis reveals that most events consist of dip-slip motion along near-vertical planes that strike parallel to the orientation of the mining face. These mechanisms are consistent with the expected deformation that would occur as a longwall panel advances, with the under- and over-burdens moving upwards and downwards respectively to fill the void created by mining. This further reinforces our conclusion that the events are directly induced by the mining process. Similar mechanisms have been observed during longwall mining at other sites.

46 **1. INTRODUCTION**

47 Seismicity induced by coal mining has been a common occurrence in the United Kingdom (e.g.,  
48 Redmayne, 1988). Indeed, Wilson et al. (2015) estimated that between 20 – 30% of all  
49 earthquakes recorded in the UK between 1970 – 2012 were induced by coal mining. From the  
50 late 1980s onwards the rate of coal production has declined significantly, as has the rate of  
51 associated earthquakes (Figure 1).



52  
53 *Figure 1: Deep mined coal production in the UK by year (bars) and the number of induced*  
54 *earthquakes per year associated with coal mining (grey line), as categorised by Wilson et al.*  
55 *(2015). The drop in both production and induced seismicity in 1984 is associated with the UK*  
56 *miner’s strike.*

57 Nevertheless, seismicity associated with deep coal mining still occurs in the UK. Between  
58 December 2013 – January 2014, the UK’s national seismometer network detected a series of  
59 over 40 earthquakes near to the village of New Ollerton, Nottinghamshire. The largest of these  
60 events had a magnitude of  $M_L = 1.7$ . Given the generally low levels of seismicity in the UK,  
61 the village was dubbed the “UK’s Earthquake Capital” (Turvill, 2014). The area has a history  
62 of seismic activity relating to coal mining (e.g., Bishop et al., 1993), and it was soon identified  
63 that the events were likely to be associated with longwall coal mining at the nearby Thoresby  
64 Colliery, which at the time was one of the few remaining deep coal mining sites in the UK.

65 In response to the felt earthquakes, a temporary local monitoring network of surface  
66 seismometers was deployed between the 5<sup>th</sup> February and the 30<sup>th</sup> October 2014 by the British  
67 Geological Survey (BGS). This network recorded a further 300 seismic events. The high quality  
68 of the data recorded by the local network permits a detailed study into the nature of seismicity  
69 and deformation induced by the longwall mining process.

71 *1.1 Longwall Coal Mining at Thoresby*

72 The Thoresby Colliery opened in 1925. Over the history of the site, at least 4 different seams  
73 have been mined, including the High Hazels, Top Hard, Deep Soft and Parkgate Seams, in  
74 order from shallowest to deepest: see Edwards (1967) for a stratigraphic section showing the  
75 positions of these and other seams in the region. The Deep Soft Seam was the last to be  
76 developed, with work beginning in 2010: this was the only seam being actively mined during  
77 the study period. The colliery closed entirely in mid-2015. This was for economic reasons, i.e.  
78 the low price of coal, not because of the induced seismicity.

79 The Deep Soft Seam was mined using standard longwall methods: hydraulic jacks are used to  
80 support the roof while a shearing device cuts coal from the face. As the face advances, the jacks  
81 are moved forward, allowing the roof to collapse into the cavity that is left behind. The  
82 collapsed, brecciated roof material filling this void is known as goaf (e.g. Younger, 2016). At  
83 Thoresby, each longwall panel has dimensions of approximately 300 m width, between 1,000  
84 – 3,000 m length, and approximately 2.5 m height.

85

86 *1.2 Seismicity Associated with Longwall Coal Mining*

87 Seismicity has often been associated with the longwall mining process (e.g., Cook, 1976;  
88 Gibowicz et al., 1990; Bishop et al., 1993; Stec, 2007; Bischoff et al., 2010; Sen et al., 2013).  
89 Seismic events associated with coal mining have often been divided into two categories:  
90 “mining-tectonic” activity, produced by activation of pre-existing tectonic faults, and “mining-  
91 induced” activity, directly associated with the mining excavations (e.g., Stec, 2007).

92 Observed magnitudes have typically ranged from  $0.5 < M_L < 3.5$ . At some sites event  
93 magnitudes have followed the Gutenberg and Richter (1944) distribution (e.g., Bishop et al.,  
94 1993; Kwiatek et al., 2011), while in other cases bimodal or other frequency-magnitude  
95 distributions have been observed (e.g. Stec, 2007; Hudyma et al., 2008; Bischoff et al., 2010).  
96 These non-Gutenberg-Richter distributions have been attributed to the presence of  
97 characteristic length scales (the dimensions of the mined panels, for example) that provide a  
98 control on rupture dimensions and thereby event magnitudes.

99 Analysis of event focal spheres has revealed a variety of source mechanisms in different settings  
100 (e.g., Stec, 2007; Bischoff et al., 2010; Sen et al., 2013) including: non-double-couple events,  
101 indicating a volumetric component of deformation usually associated with the roof collapse  
102 process; double-couple events showing a direct relationship to mined panels, with vertical fault  
103 planes running parallel to the mining face, on which dip-slip motion occurs; and double-couple  
104 events that correspond to regional fault orientations and *in situ* tectonic stress conditions.

105 In this paper we follow the processes developed in the aforementioned studies to characterise  
106 the seismicity induced by mining at the Thoresby Colliery. We begin by locating events,  
107 comparing the event locations to the propagation of the mining faces with time, and seismicity  
108 rates with the volume of coal extracted from the mine. We investigate the source characteristics  
109 of the events, using spectral analysis combined with event frequency-magnitude distributions  
110 to assess the length-scales of structures that have generated the observed events. We use shear-  
111 wave splitting analysis to image *in situ* stress orientations at the site, and we calculate focal  
112 mechanisms for the events to establish the orientations of fault planes and slip directions  
113 generated by the mining process.

114

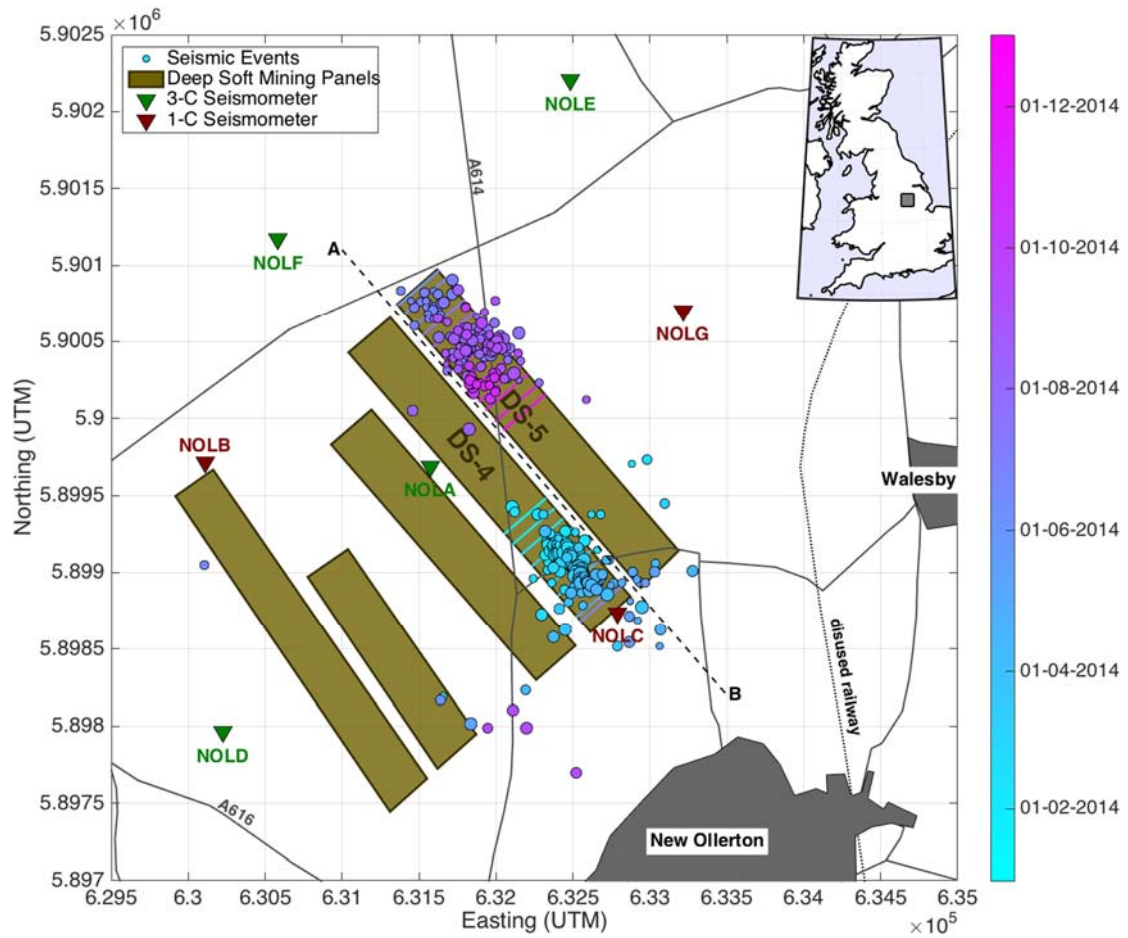
## 115 **2. EVENT DETECTION AND LOCATION**

### 116 *2.1. Monitoring array and event detection*

117 The local surface network deployed to monitor seismicity at the Thoresby Colliery comprised  
118 of 4 3-component Guralp 3ESP broadband seismometers (stations NOLA, NOLD, NOLE and  
119 NOLF) and 3 vertical-component Geotech Instruments S13J short-period seismometers  
120 (NOLB, NOLC and NOLG)). The station positions are shown in Figure 2. Events were detected  
121 using the BGS's in-house event detection algorithm, which is based on identification of peaks  
122 in running short-time/long-time averages (STA/LTA), as described by Allen (1982). A total of  
123 305 events were identified during the deployment of the local monitoring network.

124 P- and S-wave arrival times were re-picked manually for every event (e.g. Figure 3). For most  
125 event-station pairs the P-wave arrival was clear and unambiguous, and so could be accurately  
126 picked (83% of station-event pairs where a pick could be manually assigned). Stations NOLB,  
127 NOLC and NOLG were single, vertical component stations, so S-wave picks were not made  
128 for these stations. For smaller events with lower signal-to-noise ratios, clear S-wave arrivals  
129 were sometimes difficult to identify, resulting in a lower number of picks (74% of station-event  
130 pairs where a pick could be manually assigned).

131 The velocity model used to locate the events is taken from Bishop et al. (1993), and is listed in  
132 Table 1. The arrival time picks were inverted for the best-fitting location that minimises the  
133 least-squares residual between modelled and picked arrival times. The search for the best-fitting  
134 location was performed using the Neighbourhood Algorithm (Sambridge, 1999), and the  
135 modelled travel times were calculated using an Eikonal solver (Podvin and Lecomte, 1991). A  
136 map of event hypocentres is shown in Figure 2, in which the mining panels and the position of  
137 the mining face with time are also shown.



138

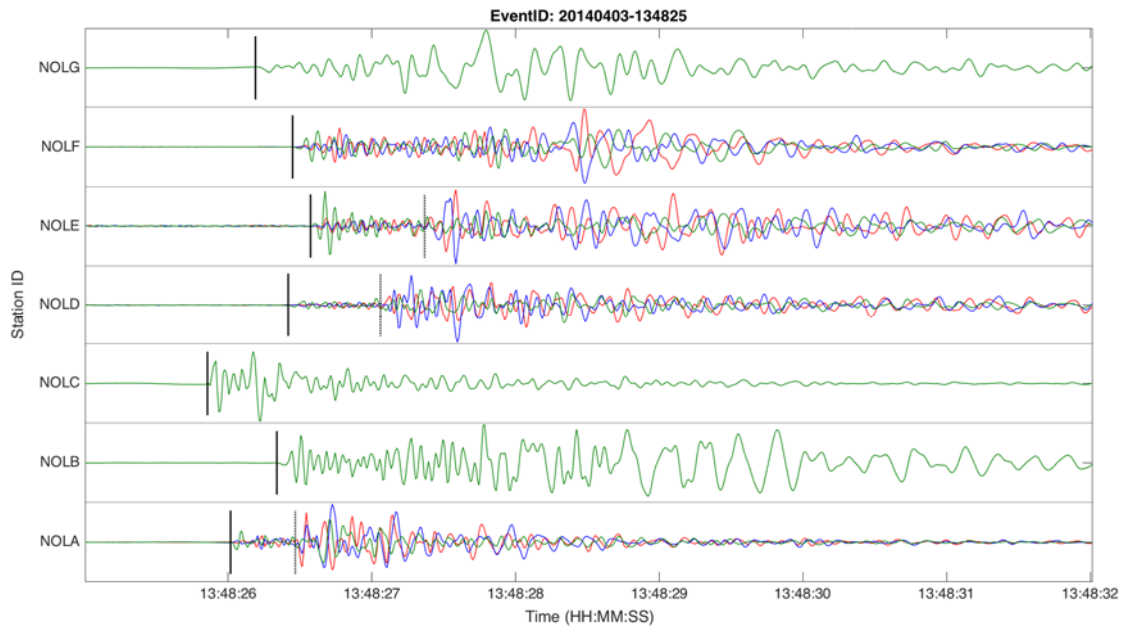
139 *Figure 2: Map of event hypocentres, with events coloured by occurrence date. Also shown are*  
 140 *the positions of the monitoring network (triangles) and the mining panels (brown rectangles).*  
 141 *Panels DS-4 and DS-5 were active during the monitoring period, and the coloured bars running*  
 142 *across these panels show the forward movement of the mining faces with time. The position of*  
 143 *the cross-section A – B (Figure 5) is marked by the dashed line.*

144

| Layer No. | Depth to Layer Top (m) | $V_P$ ( $ms^{-1}$ ) | $V_S$ ( $ms^{-1}$ ) |
|-----------|------------------------|---------------------|---------------------|
| 1         | 0                      | 1900                | 1280                |
| 2         | 60                     | 2750                | 1540                |
| 3         | 135                    | 3100                | 1740                |
| 4         | 275                    | 3500                | 1970                |
| 5         | 1019                   | 4200                | 2360                |
| 6         | 1351                   | 5250                | 2920                |
| 7         | 2751                   | 6000                | 3370                |

145 *Table 1: 1D, layered, isotropic velocity model used to locate events. Model is based on that used by*  
 146 *Bishop et al. (1993).*

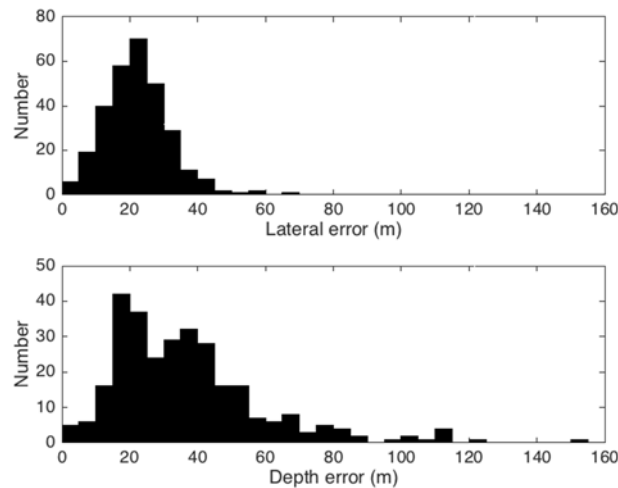
147



148

149 *Figure 3: Recorded waveforms for a larger event ( $M_L = 1.3$ ). The N (red), E (blue) and Z (green)*  
 150 *components for each station are overlain. Stations NOLB, NOLC and NOLG are single (Z) component*  
 151 *stations. The P- and S-wave picks are marked by the solid and dashed tick marks.*

152 In Figure 4 we show histograms of the event location uncertainties laterally and in depth. Note  
 153 that these uncertainties pertain solely to the residuals between picked and modelled arrival  
 154 times, and do not account for velocity model uncertainties. The velocity model used is based  
 155 on limited site-specific data, relying mainly on regional seismic refraction surveys (Bishop et  
 156 al., 1993).



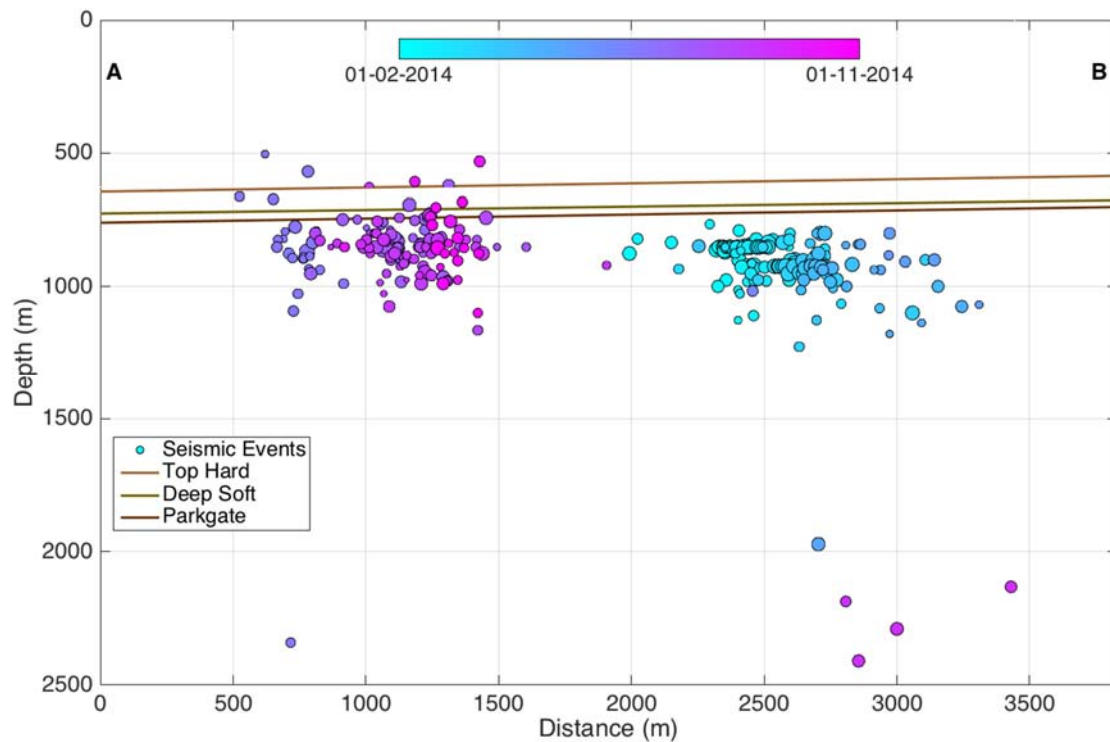
157

158 *Figure 4: Histograms showing the lateral and depth uncertainties for the located events.*

159 A brief sensitivity analysis suggested that velocity model uncertainties of up to 10% may affect  
 160 depth locations by as much as 150m, while lateral locations are relatively unaffected. This  
 161 reflects the geometry of the array, which provides reasonable azimuthal coverage but with

162 surface stations only, such that an uncertain velocity model will primarily affect the event  
163 depths.

164 Figure 5 shows a cross-section of event depths relative to the coal seams. We note that, while  
165 it appears that the events are located below the seam depths, given the likely velocity model  
166 uncertainties, it is not possible to rule out that these events are actually located at the same  
167 depths as the Deep Soft Seam being mined.



168

169 *Figure 5: Events depths shown along cross-section A – B (see Figure 2). The positions of the*  
170 *Top Hard, Deep Soft and Parkgate Seams are also marked. Note that velocity uncertainties*  
171 *mean that the event depths may not be particularly well constrained.*

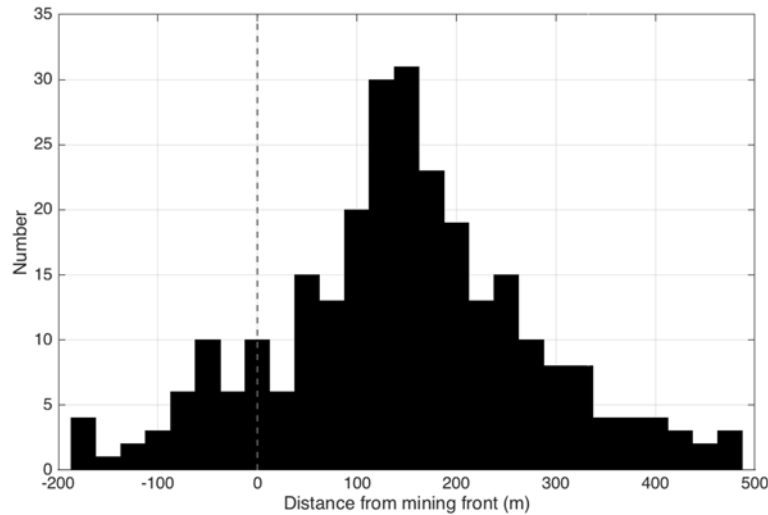
## 172 2.2. Event Locations with Respect to Mining Activities

173 The positions of the mining panels, and the progress of the mining face with time, have been  
174 provided by the UK Coal Authority in their Mine Abandonment Plans (2017). The position of  
175 the mining face with respect to the events can be seen in Figure 2. It is immediately apparent  
176 that the event locations are tracking the position of the face as it moves SE along panel DS-4,  
177 before switching to DS-5 and again tracking the mining front to the SE. The monitoring period  
178 ceases when the events have propagated approximately half-way along the length of panel DS-  
179 5.

180 We investigate the position of events in relation to the mining face in greater detail in Figure 6,  
181 which shows a histogram of event positions relative to the mining face, along an axis parallel  
182 to the mining panels. Most events are found to occur ahead of the face, with most events



183 occurring within 300m of the face. This close correlation between events and the mining face  
184 implies that the events are being directly induced by mining activities, as opposed to the  
185 activation of pre-existing tectonic features, in which case we would expect the events to align  
186 along an activated fault. As per the categorisation described by Stec (2007), we characterise  
187 these as mining-induced events.



188

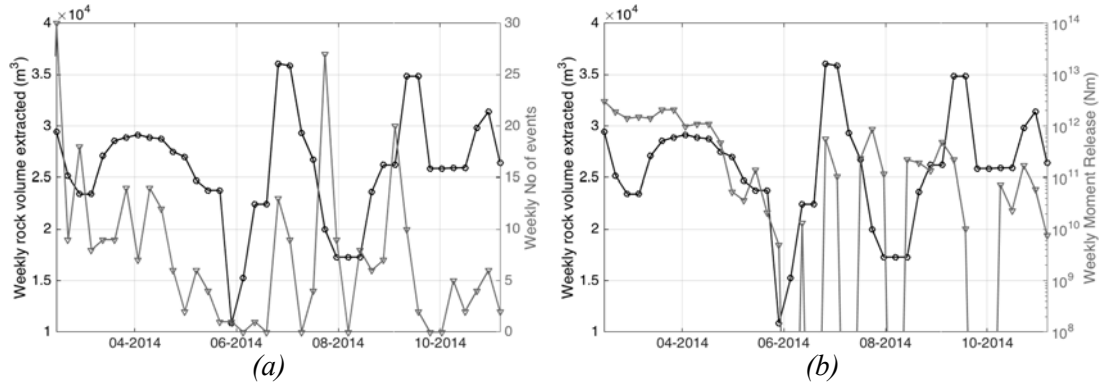
189 *Figure 6: Histograms showing the lateral position of each event relative to the mining face at the time*  
190 *of event occurrence, where a positive distance represents events occurring in advance of the face.*

191 However, we also note small cluster of 5 events that is found at greater depths (>2,000m), to  
192 the SW of the DS-4 panel. 4 of these 5 events occurred within a single 7-hour period.  
193 Establishing the causality of these events is more difficult. It is possible that these events have  
194 been have been triggered by the static transfer of stress changes to greater depths, leading to  
195 fault activation. As per the Stec (2007) categorisation, these may be mining-tectonic events.  
196 However, it is not possible to rule out that these deeper events may in fact have a natural origin.

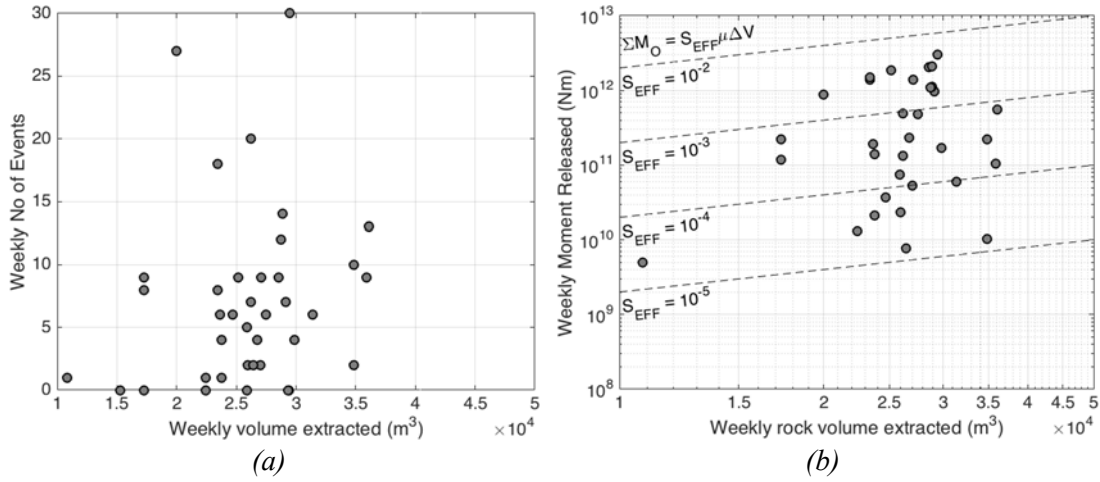
### 197 **3. CORRELATION BETWEEN SEISMICITY AND MINING RATES?**

198 In Figure 7 we show the volume of rock removed from the mine on a weekly basis ( $\Delta V$ ), the  
199 number of events per week ( $N_E$ ), and the cumulative seismic moment ( $\Sigma M_O$ ) released per week.  
200 The volume of rock removed per week is estimated from the forward progress of the mining  
201 face, multiplied by its dimensions (width and height). To further investigate any correlation  
202 between the extracted volume and seismicity, in Figure 8 we cross-plot these parameters. From  
203 Figure 8 it is apparent that there is little immediate correlation between  $\Delta V$  and  $N_E$  and  $\Sigma M_O$  on  
204 a weekly basis.

205



206 Figure 7: Weekly rock volume extracted (black lines) compared with (a) the weekly number of recorded  
 207 events and (b) the weekly cumulative seismic moment released (grey lines).



208 Figure 8: Cross-plots examining potential correlation between weekly rock volume extracted and the  
 209 weekly number of recorded events (a) and the weekly cumulative seismic moment released (b). In (b),  
 210 the dashed lines show the expected relationship for given values of  $S_{EFF}$ .

211 McGarr (1976) posited a linear relationship between  $\Delta V$  and  $\Sigma M_O$ :

$$212 \quad \Sigma M_O \approx \mu \Delta V, \quad (1)$$

213 where  $\mu$  is the rock shear modulus. This relationship corresponds to the situation whereby all  
 214 of the deformation produced by the volume change is released seismically. In reality, much of  
 215 the deformation may occur aseismically. As such, Hallo et al. (2014) proposed a modification  
 216 to this relationship via a “seismic efficiency” term,  $S_{EFF}$ , which describes the portion of the  
 217 overall deformation that is released as seismic energy:

$$218 \quad \Sigma M_O \approx S_{EFF} \mu \Delta V \quad (2)$$

219 In some of the most well-known cases of induced seismicity, values of  $S_{EFF}$  have been close to  
 220 1 (e.g. McGarr, 2014). However, these cases represent outliers: during most industrial  
 221 operations  $S_{EFF}$  is much less than 1 (e.g., Hallo et al., 2014). The dashed lines in Figure 8(b)  
 222 show the relationship between  $\Delta V$ ,  $\Sigma M_O$  and  $S_{EFF}$ , assuming a generic value of  $\mu = 20$  GPa. We  
 223 note that the observed moment release rates correspond to values of  $S_{EFF}$  between 0.01 to

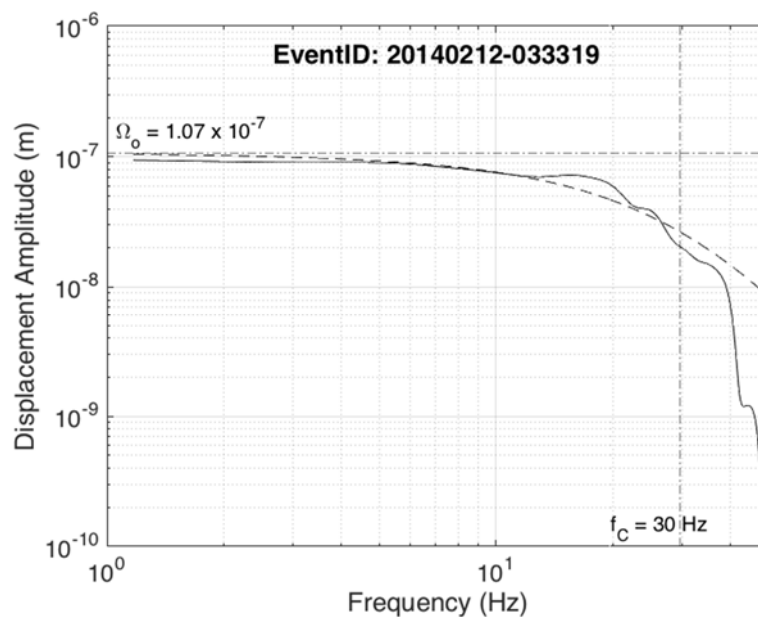
224 0.00001, implying that most of the deformation induced by the mining is released aseismically.  
225 This is typical for many cases of seismicity induced by a variety of industrial activities (e.g.  
226 Maxwell et al., 2008; Hallo et al., 2014)

## 227 **4. EVENT MAGNITUDES AND FREQUENCY-MAGNITUDE DISTRIBUTIONS**

### 228 *4.1 Moment Magnitude Calculation*

229 Local magnitudes for the Thoresby Colliery seismicity have been computed by Butcher et al.  
230 (2017), who found that the UK's existing local magnitude scale (Ottmöller and Sargeant,  
231 2013) is not appropriate for use when sources and receivers are within a few kilometres of each  
232 other. This is because for nearby receivers, the raypath will be predominantly through the softer,  
233 more attenuative sedimentary cover, rather than the underlying crystalline crustal rocks, as will  
234 be the case for receivers that are more distant to the event. Butcher et al. (2017) have developed  
235 an alternative local magnitude scale based on the Thoresby events, which has been recalibrated  
236 to ensure consistency between magnitude measurements made on nearby stations and those  
237 made using the UK's permanent national monitoring network, the nearest stations of which  
238 were some distance from the Thoresby site.

239 However, our aim here is to investigate event magnitude distributions in order to understand  
240 the length scales of structures being affected by the mining process. This therefore requires the  
241 use of moment magnitudes, since seismic moment can be directly related to rupture dimensions.  
242 We compute moment magnitudes by fitting a Brune (1970) source model to the observed S-  
243 wave displacement amplitude spectra (Figure 9), following the method described by Stork et  
244 al. (2014). The seismic moment is determined from the amplitude of the low-frequency plateau,  
245  $\Omega_0$ .



247 *Figure 9: Example displacement spectrum used to estimate moment magnitudes. The solid line*  
248 *shows the observed spectrum, while the dashed line shows the best-fit Brune (1970) source*  
249 *model. The dot-dash lines show the  $f_C$  and  $\Omega_0$  values for this model.*

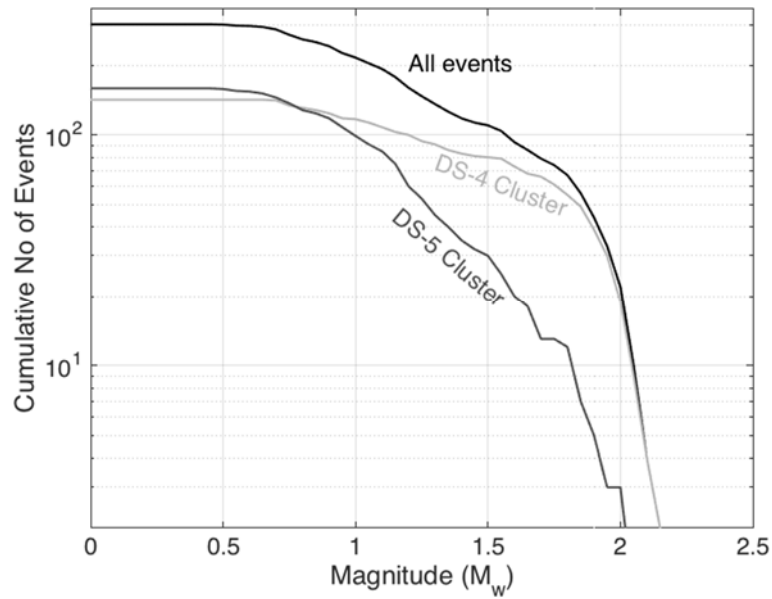
250 Ideally, the measured corner frequency,  $f_C$ , of the displacement spectra could be used to  
251 determine the rupture length. However, to robustly image the corner frequency, it must be  
252 significantly lower than the Nyquist frequency,  $f_N$  of the recording system – Stork et al. (2014)  
253 recommend that  $f_N > 4f_C$  to obtain robust estimates of  $f_C$ . The recording systems at Thoresby  
254 had sampling rates of 100 Hz, so  $f_N = 50$  Hz.

255 We can use generic values for stress drop and rupture lengths to establish the expected corner  
256 frequencies for events with  $M_W < 1$ . Using the relationships between rupture dimensions,  
257 seismic moment and stress drop given by Kanamori and Brodsky (2004), assuming a stress  
258 drop of 5 MPa and a rupture velocity of 2,000 m/s, the resulting corner frequency  $f_C \approx 30$  Hz.  
259 Evidently, the  $f_N > 4f_C$  criteria is not expected to hold for this particular dataset. However, our  
260 observations of event magnitudes, because they are derived from the amplitude spectra at low  
261 frequencies, are robust: we therefore use these to make inferences about the length scales of the  
262 structures that have generated the observed seismic events.

263

#### 264 *4.2. Frequency-Magnitude Distributions*

265 The observed event magnitude distribution (EMD) is shown in Figure 10. We show the EMDs  
266 for the overall dataset, as well as individually for the clusters associated with the DS-4 and DS-  
267 5 panels. The overall dataset is not well described by the Gutenberg and Richter (1944)  
268 distribution  $\log_{10} N(M) = a - bM$ , where  $N(M)$  is the cumulative number of events larger than  
269 a given magnitude  $M$ , and  $a$  and  $b$  are constants to be determined. Such a distribution would be  
270 represented by a straight line in  $M$  vs  $\log_{10}(N)$  space. We note that the apparent limit on the  
271 largest event size is not an artefact of a short measuring period: while the local array was  
272 removed in October 2014, the area continues to be monitored by the BGS National  
273 Seismometer Array, which has an estimated detection capability across the UK of magnitude  $>$   
274 2. Larger events occurring after the study period would therefore be detectable, but no such  
275 events have occurred.



276

277 *Figure 10: Observed frequency-magnitude distributions for the full event population (black),*  
 278 *as well as for the DS-4 (light grey) and DS-5 (dark grey) clusters individually.*

279 However, fault length and/or earthquake magnitude distributions that are constrained at some  
 280 upper limit, leading to a fall-off from the power law relationship at large values, have been  
 281 suggested by a number of authors. At the largest scale, Richter (1958) argues that “a physical  
 282 upper limit to the largest possible magnitude must be set by the strength of crustal rocks, in  
 283 terms of the maximum strain which they are competent to support without yielding”. Similarly,  
 284 Pacheco et al. (1992) argue that the rupture dimensions of very large earthquakes are limited  
 285 by the thickness of the earth’s seismogenic zone (the portion of the crust that is capable of  
 286 undergoing brittle failure). For continental rift zones, Scholz and Contreras (1998) suggested  
 287 that the maximum length of normal faults would be limited by the flexural restoring stress and  
 288 friction, and found a good match between their model and faults in the East African Rift and in  
 289 Nevada. At a much smaller scale, Shapiro et al. (2013) have suggested these effects will also  
 290 apply to induced seismicity, with the maximum fault size, and therefore earthquake magnitude,  
 291 determined by the dimensions of the volume stimulated by human activities.

292 To understand the observed EMDs at Thoresby, we consider the statistical distributions of fault  
 293 rupture areas that might produce them. Typically, rupture areas are assumed to follow a self-  
 294 similar, power law distribution (e.g., Wesnousky et al., 1983; Bonnet et al., 2001). If stress  
 295 drops are assumed to be roughly constant (e.g. Abercrombie, 1995) then this power-law rupture  
 296 area distribution will result in a power-law distribution of magnitudes, i.e. the Gutenberg-  
 297 Richter distribution.

298 A cumulative power law (PL) distribution for rupture area will take the form:

299 
$$N(L) = CA^{-\alpha} , \tag{3}$$

300 where  $N(A)$  is the number of ruptures with area greater than length  $A$ ,  $\alpha$  is the power law  
 301 exponent, and  $C$  is a constant. For a PL distribution, there is no upper limit to the maximum  
 302 rupture area. Instead, if an upper limit to the rupture area is imposed, for example by the  
 303 geometry of the mining panels, then a truncated power law (TPL) distribution results  
 304 (Burroughs and Tebbens, 2001; 2002):

$$305 \quad N(A) = C(A^{-\alpha} - A_{MAX}^{-\alpha}), \quad (4)$$

306 where  $A_{MAX}$  is the maximum rupture area.

307 To simulate event magnitudes based on rupture area, we use Kanamori and Brodsky (2004):

$$308 \quad M_0 = \Delta\sigma A^{3/2}, \quad (5)$$

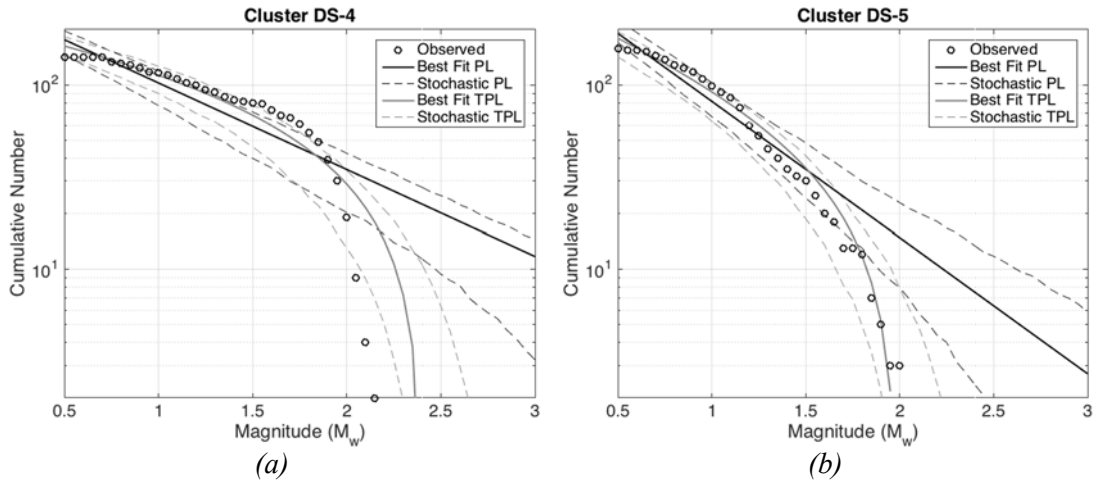
309 where  $\Delta\sigma$  is the stress drop. As discussed above, the limitation of a relatively low Nyquist  
 310 frequency means that we cannot measure the stress drop directly. Therefore, to estimate the PL  
 311 and TPL parameters that best-fit our observations, we initially assume a generic and arbitrary  
 312 stress drop of  $\Delta\sigma = 5$  MPa.

313 For each of the DS-4 and DS-5 event clusters, we perform a search over the PL and TPL  
 314 parameters, finding those that minimise the least-squares misfit between observed and  
 315 modelled EMDs. The resulting EMDs are shown as the solid lines in Figure 11, with the PL  
 316 and TPL parameters, and the misfit for each of the models, listed in Table 2. The resulting  
 317 rupture area distributions are shown in Figure 12.

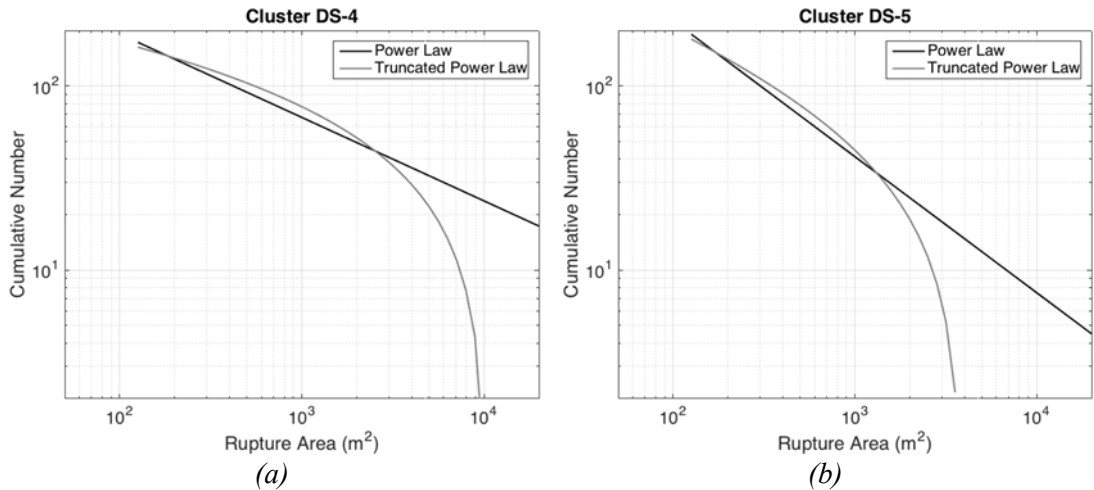
318 Having established the best-fitting PL and TPL distributions with a fixed stress drop value, we  
 319 then investigate the impact of a variable range of  $\Delta\sigma$ . We do this in a stochastic manner,  
 320 simulating rupture area distributions based on the PL and TPL parameters, assigning stress  
 321 drops randomly from a uniform distribution of  $0.1 < \Delta\sigma < 20$  MPa. We repeat this process over  
 322 100 iterations, and in Figure 11 the dashed lines show the range encompassing  $\pm 2$  standard  
 323 deviations around the resulting mean EMD. From Figure 11 we observe that both event  
 324 populations are clearly better modelled by a TPL rupture area distribution, even when stochastic  
 325 variation in  $\Delta\sigma$  is considered.

|             | <i>Dist. Type</i> | $\alpha$ | $C$  | $A_{MAX}$ | <i>Misfit</i> |
|-------------|-------------------|----------|------|-----------|---------------|
| <b>DS-4</b> | PL                | 0.47     | 1707 | NA        | 5.46          |
|             | TPL               | 0.1      | 743  | 10075     | 1.23          |
| <b>DS-5</b> | PL                | 0.74     | 6861 | NA        | 3.05          |
|             | TPL               | 0.38     | 1536 | 3870      | 0.86          |

326 Table 2: Best fitting power law and truncated power law distributions for each of the DS-4 and  
 327 DS-5 clusters, and the resulting normalised misfits.



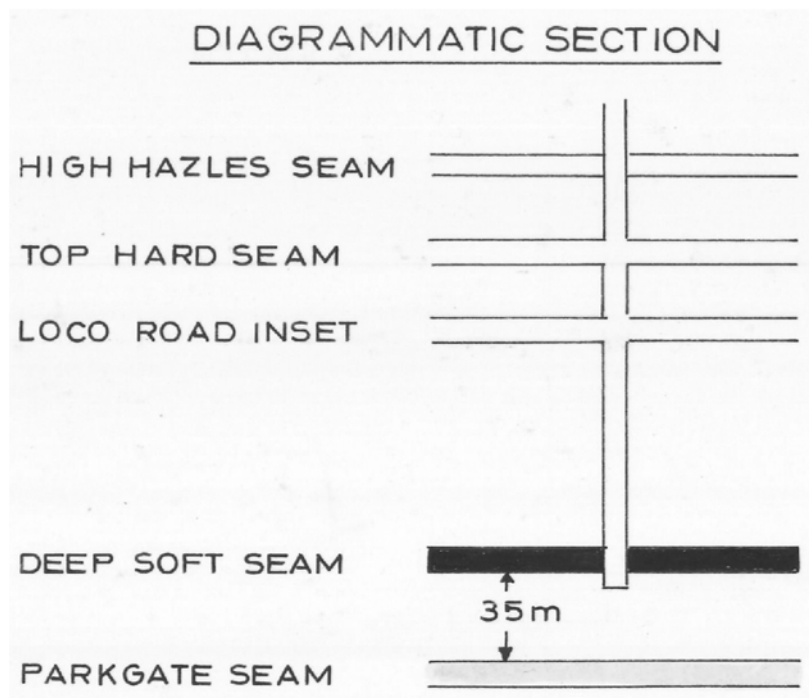
328 Figure 11: Fitting PL (black) and TPL (grey) rupture area distributions to the DS-4 (a) and  
 329 DS-5 (b) EMDs. Observed EMDs are shown by black circles. The solid lines show the best  
 330 fitting models for a fixed  $\Delta\sigma$  value, while the dashed lines show  $\pm 2$  standard deviations when  
 331  $\Delta\sigma$  is varied stochastically.



332 Figure 12: Best fitting rupture area PL (black) and TPL (grey) distributions for the DS-4 (a)  
 333 and DS-5 (b) clusters.

334 Based on these results, it is worth examining whether the best fitting values for  $A_{MAX}$  correspond  
 335 to any length-scales associated with the mining activities. There are two length scales in play  
 336 that might affect rupture dimensions: the width of the mining face (approximately 300 m); and  
 337 the separations between (1) the underlying Parkgate Seam, which is 35 m below the Deep Soft  
 338 (Figure 13), and (2) the overlying Top Hard Seam, which is approximately 110 m above the  
 339 Deep Soft. Both seams have already been mined throughout our study area. The voids left by  
 340 the longwall mining of these seams will be filled with goaf, the rubble and detritus created as  
 341 the roof collapses behind the mining face. It is difficult to envisage a mechanism by which  
 342 ruptures could propagate through such a rubble-filled void.

343 Assuming circular ruptures, areas of 10075 and 3870 m<sup>2</sup> correspond to rupture radii of 57 and  
344 35 m. The larger dimension radius is therefore roughly equivalent to a circular rupture  
345 extending from the Deep Soft to the Top Hard. Alternatively, assuming a rectangular rupture,  
346 the DS-4  $A_{MAX}$  value could correspond to a rupture with dimensions of approximately 35 × 300  
347 m, equivalent to a rupture extending from the Deep Soft to the Parkgate, across the length of  
348 the mined face. In reality, ruptures will not be rectangular nor circular. Nevertheless, the general  
349 agreement between the dimensions of the maximum rupture area and these distances leads us  
350 to suggest that the presence of the overlying and underlying Top Hard and Parkgate seams is  
351 indeed limiting the rupture dimensions. Given the similarities between these dimensions, it is  
352 not possible to determine whether one of these features in particular is controlling the maximum  
353 rupture area. Indeed, it is likely that all three features: the width of the mining face; the distance  
354 to the underlying Parkgate Seam; and the distance to the overlying Top Hard Seam, are all  
355 playing a role in limiting the maximum rupture dimensions.



356

357 *Figure 13: Diagrammatic section showing the spacing between the Deep Soft Seam, and the*  
358 *underlying Parkgate Seam, which has already been mined out across the study area. Image*  
359 *taken from UK Coal Authority Mine Abandonment Plans (2017).*

360

## 361 **5. SEISMIC ANISOTROPY AND SHEAR-WAVE SPLITTING**

362 Shallow crustal anisotropy can be generated by several mechanisms, including: alignment of  
363 macroscopic fracture networks; the preferential alignment of microcracks due to anisotropic

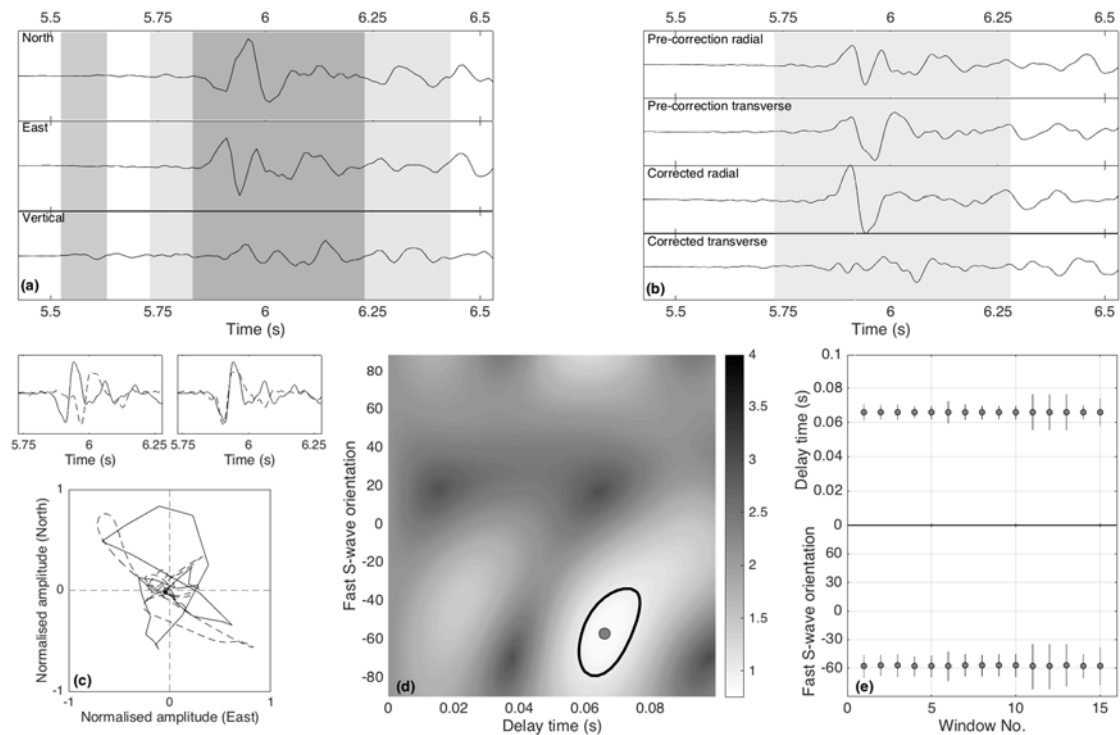


364 stress field (in practice, the microscopic and macroscopic effects often combine, as both larger-  
365 scale fracture networks and microcracks are preferentially opened or closed by the same stress  
366 field); and by the alignment of sedimentary bedding planes.

367 Shear-wave splitting (SWS), where the velocity of a shear-wave is dependent upon the direction  
368 of travel and the polarity of the wave, is an unambiguous indicator of seismic anisotropy, and  
369 has been used previously to image stress changes induced by mining activities (Wuestefeld et  
370 al., 2011). Shear-waves that propagate near-vertically will not be sensitive to horizontally-  
371 layered sedimentary fabrics, which produce Vertically-Transverse-Isotropy (VTI) symmetry  
372 systems. Instead, in the absence of other major structural fabrics, the fast shear wave  
373 polarisation orientation can be treated as a proxy for the direction of maximum horizontal stress  
374 (e.g., Boness and Zoback 2006).

375 We perform SWS measurements on the Thoresby data. Accurate SWS measurements can only  
376 be obtained within the “S-wave window” (Crampin and Peacock 2008), because arrivals at an  
377 incidence angle greater than  $\sim 35^\circ$  from vertical may be disturbed by S-to-P conversions at the  
378 free surface. This constraint limits the available data considerably, such that events within the  
379 S-wave window are found only on station NOLA, and for only 28 of the recorded events.

380 We perform the SWS measurement using the automated cluster-based approach described by  
381 Teanby et al. (2004). Where larger datasets are studied, automated quality assessments such as  
382 that described by Wuestefeld et al. (2010) can be used, but in this case, given the small sample  
383 size, the quality of measurements were assessed manually. Of the 28 arrivals within the S-wave  
384 window at NOLA, 9 provided good-quality, robust results according to the diagnostic criteria  
385 specified by Teanby et al. (2004). This is a typical rate-of-return for such studies given the  
386 relatively low magnitude (and therefore signal-to-noise) of the events. An example of a robust  
387 SWS measurement is provided in Figure 14



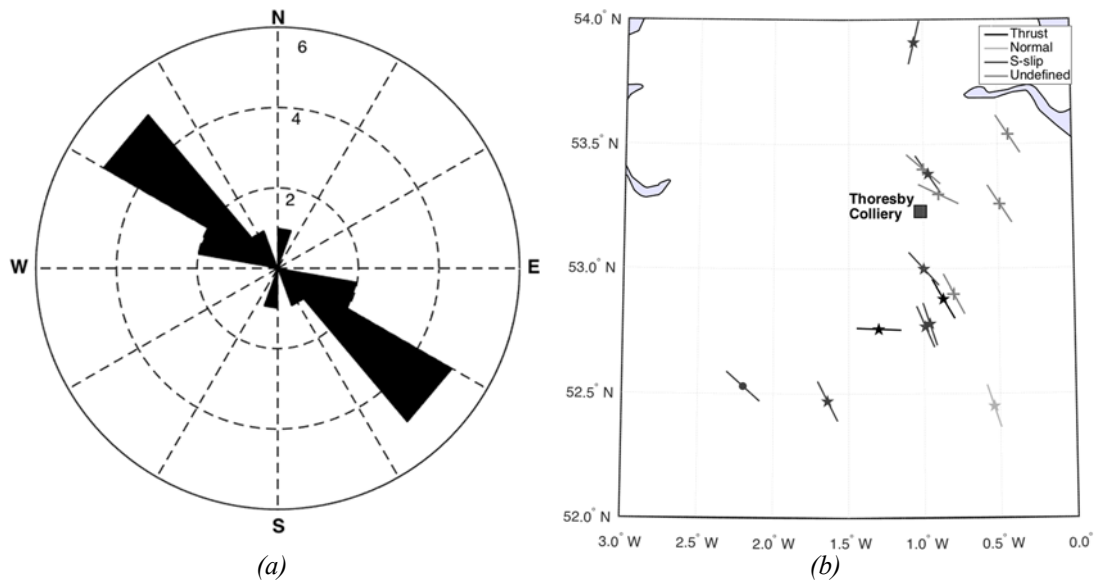
388

389 *Figure 14: Example shear-wave splitting measurement using the method described by Teanby et al.*  
 390 *(2004). In (a) we plot the N, E and Z components of the recorded waveforms, where P- and S-wave*  
 391 *windows are highlighted by the shaded areas. In (b) we plot the radial and transverse components prior*  
 392 *to and after the splitting correction, where the aim of the correction is to minimise energy on the*  
 393 *transverse component. In (c) we plot the waveform particle motions before (solid lines) and after (dashed*  
 394 *lines) correction. In (d) we plot the error surfaces of the correction method as a function of delay time*  
 395 *and fast direction normalised such that the 95% confidence interval (highlighted in bold) is 1. In (e) we*  
 396 *plot the best-fit delay times and fast directions that result from choosing different S-wave window start*  
 397 *and end times (as indicated by the light-grey shaded zone of (a)).*

398 In Figure 15a we show the measured fast directions in the form of an angle histogram. A  
 399 dominant fast direction striking NW-SE is clearly observed. The mean fast direction azimuth  
 400 is  $130^\circ$ . No temporal variations in SWS fast directions or percentage anisotropy were observed.  
 401 The mean delay time was 43 ms, and the mean percentage S-wave anisotropy was 6.8%.

402 In Figure 15b we compare the measured fast S-wave orientations with independent  
 403 measurements for  $S_{Hmax}$  taken from the World Stress Map database (Heidbach et al., 2008).  
 404 These measurements, mainly from borehole breakouts and hydraulic fracturing tests, also  
 405 indicate an approximate regional  $S_{Hmax}$  strike that is to the NW-SE. We conclude that the mean  
 406 measured S-wave fast polarity of  $130^\circ$  can be used as a proxy for  $S_{Hmax}$  at this site.

407

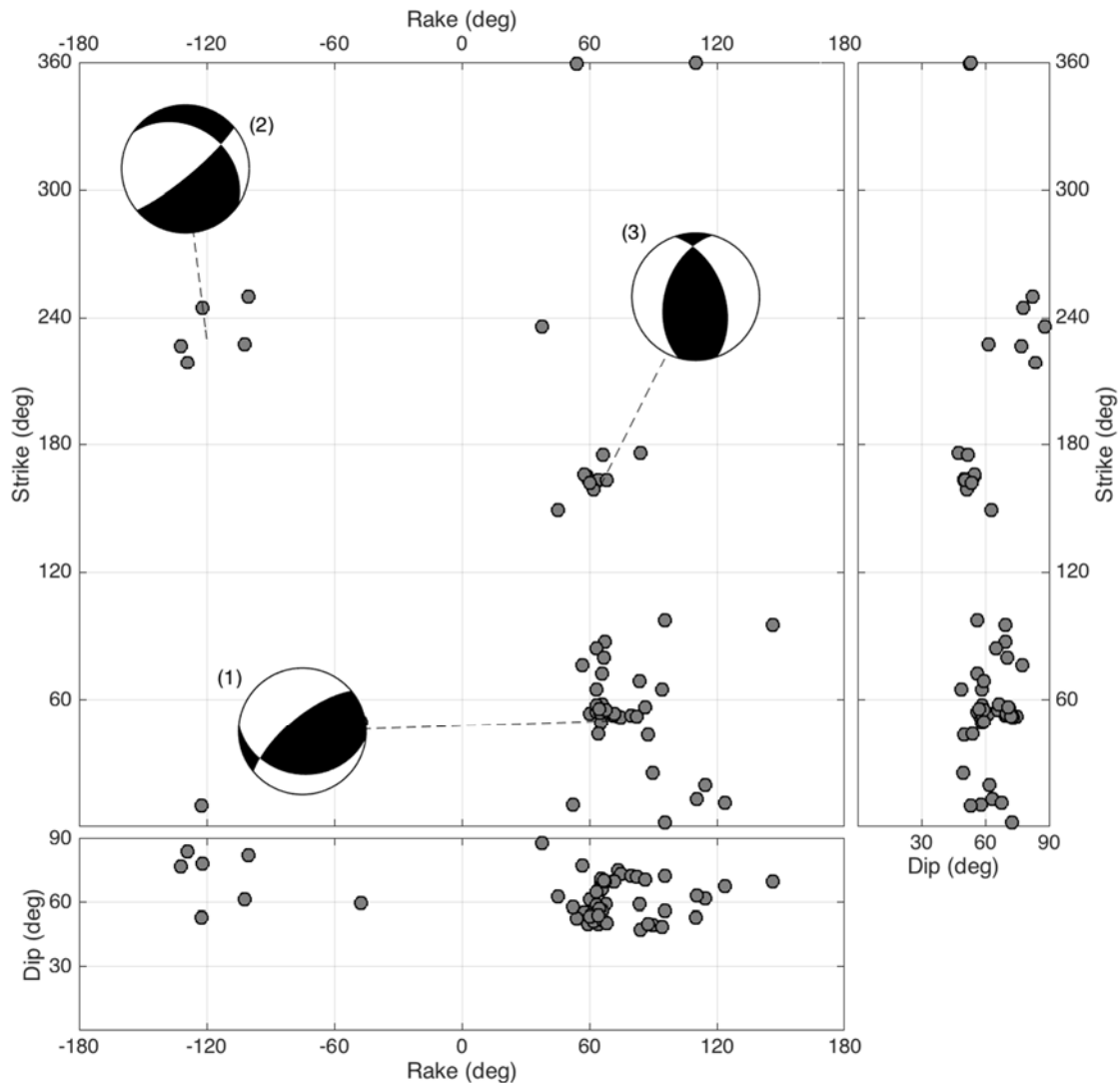


408 Figure 15: SWS and stress anisotropy. In (a) we plot an angle histogram of the measured SWS fast  
 409 directions. In (b) we show regional measurements of  $S_{Hmax}$  from the World Stress Map database  
 410 (Heidbach et al., 2008): '+' symbols represent borehole breakouts, 'o' symbols represent focal  
 411 mechanisms, and '★' symbols represent hydraulic fracturing data. The Thoresby site is marked by the  
 412 red square. Measurements are coloured by whether they represent a thrust, normal or strike-slip stress  
 413 regime (if known).

## 414 6. SOURCE MECHANISMS

415 We compute event focal mechanisms by inverting the observed P-wave polarities and relative  
 416 P-wave,  $S_H$  and  $S_V$  wave amplitudes for the best fitting double-couple source mechanism. In  
 417 doing so, we preclude the possibility of non-double-couple sources in our inversion, as might  
 418 be anticipated during mining-induced seismicity. We do this because the monitoring array  
 419 consists of only 4 3-C and 3 1-C stations, which limits our ability to robustly constrain non-  
 420 double-couple events. However, we note that the recovered mechanisms do a reasonable job of  
 421 fitting the observed polarities, i.e. non-double-couple sources do not appear to be necessary to  
 422 match the majority of our observations.

423 Of the 305 events, a total of 65 had sufficient signal-to-noise ratios such that P-wave polarities  
 424 could be robustly assigned, and produced reliable and consistent source mechanisms. These  
 425 strikes, dips and rakes for these events are plotted in Figure 16. We note 3 main clusters of  
 426 event types, representative source mechanisms for which are also plotted.



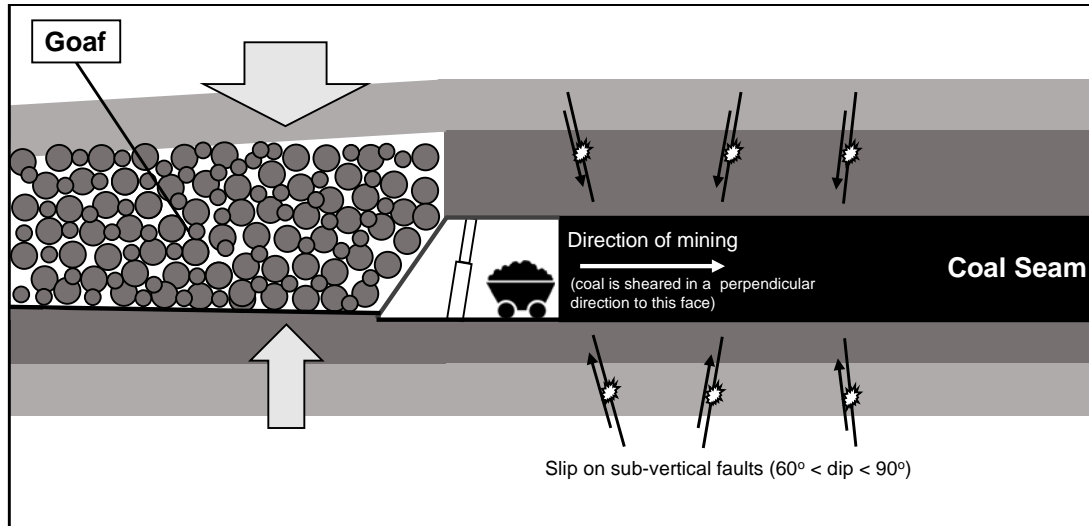
427

428 *Figure 16: Source mechanisms (strike, dip and rake) for each event for which a reliable*  
 429 *mechanism could be obtained. Three main clusters of mechanisms can be identified,*  
 430 *representative focal spheres for which are shown. These spheres are upper-hemisphere*  
 431 *projections where the compressive quadrants are shaded black.*

432 The most common source mechanism type (numbered 1 in Figure 16) consists of events with  
 433 strikes of approximately  $50^\circ$ , high angles of dip, and rakes of between  $60^\circ - 90^\circ$ . This source  
 434 mechanism orientation corresponds to near-vertical planes whose strikes match the strike of the  
 435 mining face, on which dip-slip movement occurs, with the side of the fault that is towards the  
 436 mine moving downwards.

437 A second, less populous source mechanism type (numbered 2 in Figure 16) shows similar  
 438 strikes and dips, but with the opposite sense of movement such that the side of the fault towards  
 439 the mining face moves upwards. Similar event mechanisms – near-vertical failure planes  
 440 striking parallel to the mining face with upward and downward dip-slip motion – were observed  
 441 by Bischoff et al. (2010) for longwall mines in the Ruhr Area, Germany, and we share their

442 geomechanical interpretation for these events (Figure 17). As the coal is mined, the surrounding  
 443 rock mass will collapse to fill the void. This will result in downward motion of the overlying  
 444 rock (as per source mechanism type 1), and upward motion of the underlying rock (as per source  
 445 mechanism type 2) along vertical planes that run parallel to the mining face.



446

447 *Figure 17: Geomechanical interpretation of the observed source mechanisms. As the*  
 448 *surrounding rocks move to fill the void created by mining, dip-slip motion occurs on near-*  
 449 *vertical slip planes oriented parallel to the mining face. Adapted from Bischoff et al. (2010).*

450 A third type of source mechanism is also observed (numbered 3 in Figure 16), with thrust-type  
 451 mechanisms occurring on steeply-dipping planes that strike approximately north-south. It  
 452 is possible that they result from the interaction between mining activities and pre-existing  
 453 structures in the area, since the N-S orientation of these planes does not match the orientation  
 454 of any feature in the mine.

455 Using the source mechanisms for all events, we use the STRESSINVERSE iterative joint  
 456 inversion algorithm described by Vavrycuk (2014) to estimate the orientations of principal  
 457 stresses and the shape ratio,  $R$  (Gephart and Forsyth, 1984):

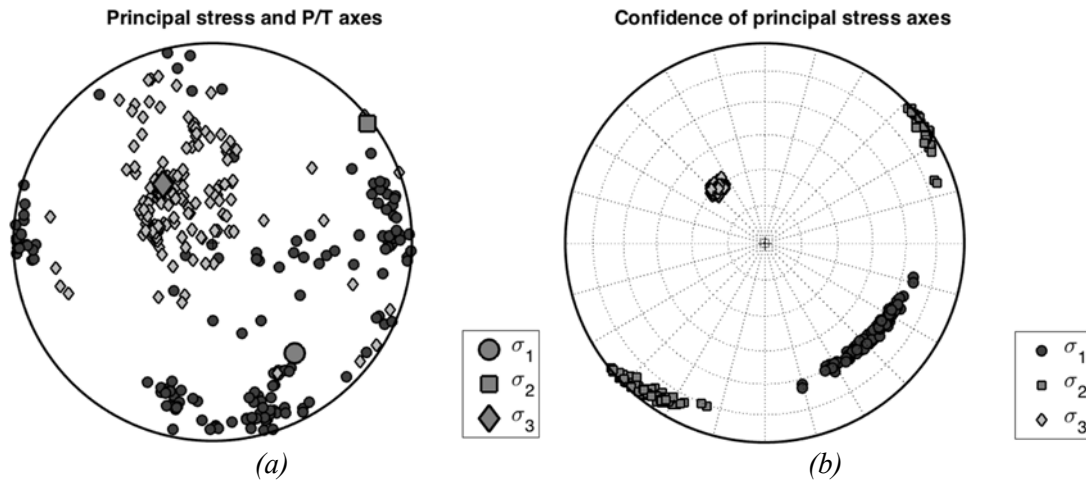
$$458 \quad R = \frac{\sigma_1 - \sigma_2}{\sigma_1 - \sigma_3}, \quad (4)$$

459 where  $\sigma_1$ ,  $\sigma_2$ , and  $\sigma_3$  represent the maximum, intermediate and minimum principal stresses. The  
 460 results of this inversion are listed in Table 3, and shown in Figure 18. We note that the resulting  
 461 maximum horizontal stress is sub-horizontal, with an azimuth of  $144^\circ$ . This is consistent, within  
 462 error, with the maximum horizontal stress orientation estimated from SWS analysis. This  
 463 implies that, while the orientations of the slip planes are consistent with the geometry of the  
 464 mining activities, the resulting deformation is also consistent with the regional *in situ* stress  
 465 conditions.

| <i>Stress</i> | <i>Azimuth</i> | <i>Plunge (down from horizontal)</i> | <i>Shape Ratio (R)</i> |
|---------------|----------------|--------------------------------------|------------------------|
| $\sigma_1$    | 144°           | 31°                                  | 0.17                   |
| $\sigma_2$    | 52°            | 2°                                   |                        |
| $\sigma_3$    | 319°           | 59°                                  |                        |

467 Table 3: Principal stress orientations and Shape Ratio ( $R$ ) as inverted from event source mechanisms

468



469 Figure 18: Stress tensor inversion results using the *STRESSINVERSE* algorithm (Vavrycuk,  
 470 2014). In (a) we show a lower hemisphere projection of the  $P$  (dark grey  $\circ$ ) and  $T$  (light grey  
 471  $\diamond$ ) axes for every event, with the overall estimate for the  $\sigma_1$ ,  $\sigma_2$ , and  $\sigma_3$  axes marked by a large  
 472  $\circ$ ,  $\square$ , and  $\diamond$ , respectively. In (b) we show confidence limits for the principle stress axes,  
 473 assuming  $\pm 15^\circ$  error in source mechanism orientations.

474 **6. CONCLUSIONS**

475 In this paper, we characterise the seismicity recorded during longwall mining of the Deep Soft  
 476 Seam at the Thoresby Colliery, Nottinghamshire, U.K.. A local monitoring network was  
 477 installed for 8 months, recording 305 events, with the largest event having a local magnitude  
 478 of  $M_L = 1.7$ . Event locations are found to track the advance of the mining faces, with most  
 479 events being located up to 300 m ahead of the face.

480 We conclude that these events are “mining-induced”, i.e. they are directly induced by the  
 481 mining activity, as opposed to “mining-tectonic” events, which are caused by static stress  
 482 transfer producing activation of pre-existing tectonic faults. However, comparison between  
 483 weekly mining rates and the rates of seismic activity do not show strong correlation. Moreover,  
 484 the amount of deformation released in the form of seismic events is a small percentage of the

485 overall deformation produced by the mining activities (in other words, most of the deformation  
486 is released aseismically).

487 Event magnitudes do not follow the expected Gutenberg-Richter distribution. Instead, we find  
488 that the observed magnitude distribution can be reproduced by assuming that rupture areas  
489 follow a Truncated Power Law distribution, whereby there is a limit to the maximum size of  
490 the rupture area. The observed maximum rupture area could correspond to several controlling  
491 features around the seam, including the width of the mining face, and the distances to the  
492 underlying Parkgate and overlying Top Hard seams, which have already been excavated. Our  
493 inference is that the presence of these rubble-filled voids where the excavated seams have been  
494 mined out creates a limit to the maximum rupture dimensions.

495 Event source mechanism analysis shows that most events comprise dip-slip motion along near-  
496 vertical planes that strike parallel to the orientation of the mining face. This type of deformation  
497 is the expected response to the longwall mining process, and has been observed at other  
498 longwall mining sites. The observed source mechanisms are also consistent with the orientation  
499 of *in situ* regional stresses as inferred from SWS analysis.

500

## 501 **Acknowledgements**

502 JPV and JMK are funded by the BGS/University of Bristol Strategic Partnership in Applied  
503 Geophysics. This work was performed as part of the Bristol University Microseismicity Project  
504 (BUMPS).

505

## 506 **References**

- 507 Abercrombie R.E., 1995. Earthquake source scaling relationships from -1 to 5  $M_L$  using  
508 seismograms recorded at 2.5-km depth: *Journal of Geophysical Research* 100, 24015-  
509 24036.
- 510 Allen R., 1982. Automatic phase pickers: Their present use and future prospects: *Bulletin of*  
511 *the Seismological Society of America* 72, S225-S242.
- 512 Bischoff M., Cete A., Fritschen R., Meier T., 2010. Coal mining induced seismicity in the Ruhr  
513 area, Germany: *Pure and Applied Geophysics* 167, 63-75.
- 514 Bishop I., Styles P., Allen M., 1993. Mining-induced seismicity in the Nottinghamshire  
515 coalfield: *Quarterly Journal of Engineering Geology* 26, 253-279.
- 516 Boness N.L. and Zoback M. D., 2006. Mapping stress and structurally controlled crustal shear  
517 velocity anisotropy in California: *Geology* 34, 825-828.
- 518 Bonnet E., Bour O., Odling N.E., Davy P., Main I., Cowie P., Berkowitz B., 2001. Scaling of  
519 fracture systems in geological media: *Reviews of Geophysics* 39, 347-383.
- 520 Brune J.N., 1970. Tectonic stress and the spectra of seismic shear waves from earthquakes:  
521 *Journal of Geophysical Research* 75, 4997-5009.

522 Burroughs S.M. and Tebbens S.F., 2001. Upper-truncated power laws in natural systems: Pure  
523 and Applied Geophysics 158, 741-757.

524 Burroughs S.M. and Tebbens S.F., 2002. The upper-truncated power law applied to earthquake  
525 cumulative frequency-magnitude distributions: evidence for a time independent scaling  
526 parameter: Bulletin of the Seismological Society of America 92, 2983-2993.

527 Butcher A., Luckett R., Verdon J.P., Kendall J-M., Baptie B., Wookey J., 2017. Local  
528 magnitude discrepancies for near-event receivers: Implications for the UK traffic light  
529 scheme: Bulletin of the Seismological Society of America 107, *in press*.

530 Cook N.G.W., 1976. Seismicity associated with mining: Engineering Geology 10, 99-122.

531 Crampin S. and Peacock S., 2008. A review of the current understanding of seismic shear-wave  
532 splitting in the Earth's crust and common fallacies in interpretation: Wave Motion 45, 675-  
533 722.

534 Edwards W.N., 1967. Geology of the country around Ollerton. Memoirs of the Geological  
535 Survey of Great Britain, Her Majesty's Stationery Office. Available online at:  
536 <http://pubs.bgs.ac.uk/publications.html?pubID=B01568>

537 Gephart J.W. and Forsyth D.W., 1984. An improved method for determining the regional stress  
538 tensor using earthquake focal mechanism data: Application to the San Fernando earthquake  
539 sequence: Journal of Geophysical Research 89, 9305-9320.

540 Gibowicz S.J., Harjes H-J., Schäfer M., 1990. Source parameters of seismic events at Heinrich  
541 Robert Mine, Ruhr Basin, Federal Republic of Germany: evidence for nondouble-couple  
542 events: Bulletin of the Seismological Society of America 80, 88-109.

543 Gutenberg B. and Richter C.F., 1944. Frequency of earthquakes in California: Bulletin of the  
544 Seismological Society of America 34, 185-188.

545 Hallo M., Oprsal I., Eisner L., Ali M.Y., 2014. Prediction of magnitude of the largest potentially  
546 induced seismic event: Journal of Seismology 18, 421-431.

547 Heidbach O., Tingay M., Barth, A., Reinecker J., Kurfeß D., Müller B., 2008. The World Stress  
548 Map Database Release 2008.

549 Hudyma M., Potvin Y., Allison D., 2008. Seismic monitoring of the Northparkes Lift 2 block  
550 cave – part 2 production caving: Journal of the Southern African Institute of Mining and  
551 Metallurgy 108, 421-430.

552 Kanamori H. and Brodsky E.E., 2004. The physics of earthquakes: Reports on Progress in  
553 Physics 67, 1429-1496.

554 Kwiatak G., Plenkers K., Dresen G., JAGUARS Research Group, 2011. Source parameters of  
555 picoseismicity recorded at Mponeng Deep Gold Mine, South Africa: Implications for  
556 scaling relations: Bulletin of the Seismological Society of America 101, 2592-2608.

557 Maxwell S.C., Shemeta J., Campbell E., Quirk D., 2008. Microseismic deformation rate  
558 monitoring: SPE Annual Technical Conference, Denver, SPE 116596.

559 McGarr A., 1976. Seismic moments and volume changes: Journal of Geophysical Research 81,  
560 1487-1494.

561 McGarr A., 2014. Maximum magnitude earthquakes induced by fluid injection: Journal of  
562 Geophysical Research 119, 1008-1019.

563 Ottemöller L. and Sargeant S., 2013. A local magnitude scale  $M_L$  for the United Kingdom:  
564 Bulletin of the Seismological Society of America 103, 2884-2893.

565 Pacheco J.F., Scholz C.H., Sykes L.R., 1992. Changes in frequency-size relationship from  
566 small to large earthquakes: Nature 355, 71-73.

567 Podvin P. and Lecomte I., 1991. Finite difference computation of traveltimes in very contrasted  
568 velocity models: A massively parallel approach and its associated tools: Geophysical  
569 Journal International 105, 271-284.

570 Redmayne D.W., 1988. Mining induced seismicity in UK coalfields identified on the BGS  
571 national seismograph network: in Bell F.G., Culshaw M.G., Cripps J.C., Lovell M.A. (eds),



572 *Engineering Geology of Underground Movements*, Geological Society Engineering  
573 Geology Special Publication no. 5, 405-413.

574 Richter C.F., 1958. *Elementary Seismology*. Freeman and Co., San Francisco.

575 Sambridge M., 1999. Geophysical inversion with a neighbourhood algorithm –I. Searching a  
576 parameter space: *Geophysical Journal International* 138, 479-494.

577 Sen A.T., Cesca S., Bischoff M., Meier T., Dahm T., 2013. Automated full moment tensor  
578 inversion of coal mining-induced seismicity: *Geophysical Journal International* 195, 1267-  
579 1281.

580 Scholz C.H. and Contreras J.C., 1998. Mechanics of continental rift architecture: *Geology* 26,  
581 967-970.

582 Shapiro S.A., Krüger O.S., Dinske C., 2013. Probability of inducing given-magnitude  
583 earthquakes by perturbing finite volumes of rocks: *Journal of Geophysical Research* 118,  
584 3557-3575.

585 Stec K., 2007. Characteristics of seismic activity of the Upper Silesian Coal Basin in Poland:  
586 *Geophysical Journal International* 168, 757-768.

587 Stork A.L., Verdon J.P., Kendall J-M., 2014. The robustness of seismic moment and  
588 magnitudes estimated using spectral analysis: *Geophysical Prospecting* 62, 862-878.

589 Teanby N.A., Kendall J-M., van der Baan M., 2004. Automation of shear-wave splitting  
590 measurements using cluster analysis: *Bulletin of the Seismological Society of America* 94,  
591 453-463.

592 Turvill W., 2014. Welcome to Britain's earthquake capital: Sleepy Nottinghamshire town has  
593 been hit by 36 tremors in just 50 days – and geologists say mining is to blame: *The Daily*  
594 *Mail*, accessed from [http://www.dailymail.co.uk/news/article-2548146/Welcome-Britains-  
595 EARTHQUAKE-capital-Sleepy-Nottinghamshire-town-hit-36-tremors-just-50-days-  
596 geologists-say-mining-blame.html](http://www.dailymail.co.uk/news/article-2548146/Welcome-Britains-EARTHQUAKE-capital-Sleepy-Nottinghamshire-town-hit-36-tremors-just-50-days-geologists-say-mining-blame.html) on 21.01.2017.

597 UK Coal Authority Mine Abandonment Plans, 2017. Mine Abandonment Plans are available  
598 upon application to the UK Coal Authority. See [https://www.gov.uk/guidance/coal-mining-  
599 records-data-deeds-and-documents](https://www.gov.uk/guidance/coal-mining-records-data-deeds-and-documents)

600 Vavrycuk, V., 2014. Iterative joint inversion for stress and fault orientations from focal  
601 mechanisms: *Geophysical Journal International* 199, 69-77.

602 Wesnousky S.G., Scholz C.H., Shimazaki K., Matsuda T., 1983. Earthquake frequency  
603 distribution and the mechanics of faulting: *Journal of Geophysical Research* 88, 9331-9340.

604 Wilson M.P., Davies R.J., Foulger G.R., Julian B.R., Styles P., Gluyas J.G., Almond S., 2015.  
605 Athropogenic earthquakes in the UK: a national baseline prior to shale exploitation: *Marine*  
606 *and Petroleum Geology* 68, 1-17.

607 Wuestefeld A., Al-Harrasi O., Verdon J.P., Wookey J., Kendall J-M., 2010. A strategy for  
608 automated analysis of passive microseismic data to image seismic anisotropy and fracture  
609 characteristics: *Geophysical Prospecting* 58, 755-773.

610 Wuestefeld A., Kendall J-M., Verdon J.P., van As A., 2011. *In situ* monitoring of rock  
611 fracturing using shear wave splitting analysis: an example from a mining setting:  
612 *Geophysical Journal International* 187, 848-860.

613 Younger P.L., 2016. How can we be sure fracking will not pollute aquifers? Lessons from a  
614 major longwall coal mining analogue (Selby, Yorkshire, UK): *Earth and Environmental*  
615 *Science Transactions of the Royal Society of Edinburgh* 106, 89-113.

616

617